Electronic Supporting Information for: The Influence of Curvature on Domain Distribution in Binary Mixture Membranes

Wei Li,[†,‡] Jan-Michael Y. Carrillo,[*,†,¶] John Katsaras,[§,‖,⊥] Bobby G. Sumpter,[†,¶] Rana Ashkar,[*,#] and Rajeev Kumar[*,†,¶]

†*Center for Nanophase Materials Sciences, Oak Ridge National Laboratory, Oak Ridge, Tennessee 37831, United States*

‡*Present address: Center for Computation & Theory for Soft Materials, Northwestern University, Evanston, Illinois 60208*

¶*Computational Chemical and Materials Sciences, Oak Ridge National Laboratory, Oak Ridge, Tennessee 37831, United States*

§*Neutron Scattering Division, Oak Ridge National Laboratory, Oak Ridge, Tennessee 37831, United States*

‖*Department of Physics and Astronomy, University of Tennessee, Knoxville, Tennessee 37996, United States*

⊥*Shull Wollan Center: a Joint Institute for Neutron Science, Oak Ridge National Laboratory, Oak Ridge, Tennessee 37831, United States*

#*Department of Physics, Virginia Polytechnic Institute and State University, Blacksburg, Virginia 24061, United States*

E-mail: carrillojy@ornl.gov; ashkar@vt.edu; kumarr@ornl.gov

Contents

1 Entropic Effects in Polymer Melts Near a Sinusoidal Surface

To understand the coupling between the conformational degrees of freedom characterized by the Kuhn segment length and the surface curvature, we consider a polymer melt containing monodisperse flexible polymers, A, each having N_A Kuhn segments of length l_A. Also, to understand the effects of surface curvature, we consider an athermal system and focus on entropic effects. For Gaussian chains, the free energy of weakly inhomogeneous polymer melts can be written as[1]

$$\frac{F}{\rho_0 k_B T} = \frac{f_0}{k_B T} + \frac{\Delta f}{k_B T} \tag{S1}$$

where ρ_0 is a reference number density and f_0 represents contributions to the free energy resulting from the translational entropy of the chains. These contributions involve local volume fractions and can be written as:

$$\frac{f_0}{k_B T} = \int d\mathbf{r} \left\{ \frac{\phi_A(\mathbf{r})}{N_A} \ln \phi_A(\mathbf{r}) \right\} \tag{S2}$$

Here, $\phi_A(\mathbf{r})$ is the local volume fraction of A at $\mathbf{r}$, which is unity far from the surface and varies from unity to zero near an impenetrable surface. Δf in Eq. S1 contains contributions to the free energy from gradients of the volume fractions and leading order terms, up to fourth order gradients in ϕ_A, and written as:[1]

$$\frac{\Delta f}{k_B T} = \frac{1}{2} \int d\mathbf{r} \left\{ b_A^2 \frac{\left[\nabla_{\mathbf{r}} \phi_A(\mathbf{r})\right]^2}{\phi_A(\mathbf{r})} + c_A^4 \frac{\left[\nabla_{\mathbf{r}}^2 \phi_A(\mathbf{r})\right]^2}{\phi_A(\mathbf{r})} - d_A^4 \frac{\left[\nabla_{\mathbf{r}}^2 \phi_A(\mathbf{r})\right] \left[\nabla_{\mathbf{r}} \phi_A(\mathbf{r})\right]^2}{\phi_A^2(\mathbf{r})} \right\} \tag{S3}$$

$$b_A^2 = \frac{l_A^2}{18}, \quad c_A^4 = \frac{N_A l_A^4}{36^2}, \quad d_A^4 = \frac{N_A l_A^4}{3240} \tag{S4}$$

To understand entropic surface effects, consider a surface (or "wall") characterized by volume fraction profile of the form

$$\phi_w(\mathbf{r}) \quad = \quad \frac{1}{2}\left[1 - \tanh\left(\frac{z - u_0(x)}{\zeta_0}\right)\right] \tag{S5}$$

so that $\phi_A(\mathbf{r}) + \phi_w(\mathbf{r}) = 1$ implies

$$\phi_A(\mathbf{r}) \quad = \quad \frac{1}{2}\left[1 + \tanh\left(\frac{z - u_0(x)}{\zeta_0}\right)\right] \tag{S6}$$

Here, $u_0(x)$ characterizes the shape of the surface along the lateral direction, and for a sinusoidal surface centered at $z = z_0, u_0(x) = z_0 + a\sin 2\pi x/\lambda$. ζ_0 characterizes the width of the surface along z direction. In the following we analyze the limit of $\zeta_0 \to 0$ to gain understanding of surface curvature effects. Also, we consider a surface containing an integral number of sinusoidal repeats so that if L_x is the total length of the surface, then L_x/λ is an integer. Using Eqs. S1, S2, S3 and S6, in the limit of $\zeta_0 \to 0$ for a surface with dimensions L_x and L_y we can write,

$$\begin{aligned} \frac{F}{\rho_0 k_B T} \quad \to \quad \frac{\Delta f}{k_B T} = \frac{R_{gA}^3 \bar{L}_x \bar{L}_y}{6 N_A \bar{\zeta}_0} \frac{1}{\bar{\lambda}} \int_0^{\bar{\lambda}} d\bar{x} \Bigg[1 + \left(\frac{\partial u_0(\bar{x})}{\partial \bar{x}}\right)^2 + \frac{1}{12}\left(\frac{\partial^2 u_0(\bar{x})}{\partial \bar{x}^2}\right)^2 \\ + \frac{1}{15\bar{\zeta}_0^2}\left\{1 + \left(\frac{\partial u_0(\bar{x})}{\partial \bar{x}}\right)^2\right\}^2 \Bigg] \end{aligned} \tag{S7}$$

In writing Eq. S7 we have used the radius of gyration of A to make lenghts dimensionless, which leads to the replacement of $\mathbf{r} \equiv \{x, y, z\}$ by $\bar{\mathbf{r}} \equiv \{\bar{x} = x/R_{gA}, \bar{y} = y/R_{gA}, \bar{z} = z/R_{gA}\}$ so that $R_{gA} = (N_A/6)^{1/2} l_A$. For a sinusoidal surface centered at $z = z_0$, plugging $u_0(x) = z_0 + a\sin 2\pi x/\lambda$ in Eq. S7 leads to

$$\frac{\Delta f}{k_B T} \quad = \quad \frac{l_A^2 L_x L_y}{36\zeta_0}\left[1 + \frac{R_{gA}^2}{15\zeta_0^2} + \frac{1}{2}\left(\frac{2\pi a}{\lambda}\right)^2\left\{1 + \frac{2R_{gA}^2}{15\zeta_0^2} + \frac{\pi^2 R_{gA}^2}{3\lambda^2} + \frac{R_{gA}^2}{20\zeta_0^2}\left(\frac{2\pi a}{\lambda}\right)^2\right\}\right] \tag{S8}$$

Eq. S8 provides useful insights into entropic effects near surfaces. First, for a planar surface so that $a = 0$, the free energy cost for creating the gradients is

$$\frac{\Delta f}{k_B T} \equiv \frac{\Delta f_{planar}}{k_B T} = \frac{l_A^2 L_x L_y}{36\zeta_0}\left[1 + \frac{R_{gA}^2}{15\zeta_0^2}\right] \tag{S9}$$

Eq. S9 implies that in a polymer blend near a sinusoidal surface containing polymers with equal number of Kuhn segments (*i.e.*, $N_A = N_B$ in a blend containing A and B), but with different Kuhn segment lengths, l_A and l_B. Polymers with lower Kuhn length segments are preferred near the surface due to the relation $\frac{\Delta f_{planar}}{k_B T} \sim l_j^2, j = A, B$. Similarly, for $l_A = l_B$ but $N_A \neq N_B$, polymers with a lower number of Kuhn segments are favored due to the dependence of Δf_{planar} on $R_{gj}^2 \sim N_j, j = A, B$. These entropic effects can lead to vertical segregation in polymer blends near planar surfaces due to differences in either Kuhn length segments or their numbers.

Near a sinusoidal surface (*i.e.*, $a \neq 0$) effects of mean curvature may be significant. In order to get an insight into how curvature in affects entropic contributions to the free energy, we first consider the limit of $a/\lambda \to 0$, which corresponds to weak-curvature as the mean curvature $\sim (\partial^2 u_0(x)/\partial x^2)^2 \sim a^2/\lambda^4$. In the limit of $a/\lambda \to 0$, Eq. S8 becomes

$$\frac{\Delta f_{a/\lambda \to 0}}{k_B T} = \frac{\Delta f_{planar}}{k_B T} + \frac{l_A^2 L_x L_y}{72\zeta_0}\left(\frac{2\pi a}{\lambda}\right)^2 \left\{1 + \frac{2R_{gA}^2}{15\zeta_0^2} + \frac{\pi^2 R_{gA}^2}{3\lambda^2}\right\} \tag{S10}$$

where Δf_{planar} is given by Eq. S9. It can be readily shown (by comparing the term proportional to a^2/λ^4 with the rest in Eq. S10) that in this limit, effects of the mean curvature are significant only for $\lambda \leq \sqrt{5}\pi\zeta_0/\sqrt{2}$, which is almost impossible to realize in experiments due to the fact that $\zeta_0 \to 0$. We now estimate the limits in which the effects of mean curvature are significant. This can be done by making sure that $\Delta f - \Delta f_{planar}$ in Eq. S8 is proportional to a^2/λ^4. This leads to limits $\lambda \ll \pi R_{gA}/\sqrt{3} = 1.81 R_{gA}$ and $a \gg \sqrt{2} R_{gA}/3 = 0.47 R_{gA}$. In these limits, Eq. S8 becomes

$$\frac{\Delta f}{k_B T} = \frac{\Delta f_{planar}}{k_B T} + \frac{l_A^4 L_x L_y}{108\zeta_0}\frac{(\pi a)^2 N_A}{\lambda^4}\left\{\frac{\pi^2}{3} + \frac{1}{20}\left(\frac{2\pi a}{\zeta_0}\right)^2\right\} \tag{S11}$$

It should be noted that the free energy cost in the limit when the effects of mean curvature are significant is proportional to $N_A l_A^4$. This implies that in a polymer blend containing chains of equal number of Kuhn segments $N_A = N_B$, the chains with lower Kuhn segment lengths cost less in the free energy and prefer to occupy strongly curved surfaces. Although local information has been integrated out in Eq. S8, the same conclusion can be inferred about sorting based on the local mean curvature from Eq. S7, and is valid for any laterally-symmetric shape of the surface.

2 Supplementary SCFT Results

2.1 Effect of conformational asymmetry on phase distribution

We study the effect of the Kuhn length ratio η_K on phase behavior of binary homopolymer blends in thin films. In Fig. S1(a), we show density profiles of the B polymer (in colormap) inside the films of $\phi_B = 0.2$ for various η_K. The system parameters of the film are $h = 0.8$, $a = 1.0$, and $\lambda = 2.56$. The blend is in the two-phase region at $\chi N = 6$ and macrophase segregation occurs inside the corrugated thin film. Here we show the system in one period of the sine curve for illustration purposes. As the emerged phase domains are not strongly correlated with each other, the morphological behavior in a larger simulation cell containing multiple periods may be different. However, the curvature effect on domain arrangement is generally the same.

At $\eta_K = 1.0$, A and B segments are conformationally symmetric. The B-rich phase (with $\phi_B > 0.2$) locates in the high curvature regions (*i.e.*, around peaks or valleys). With increasing η_K, the B polymer becomes less flexible than the A polymer and the location of

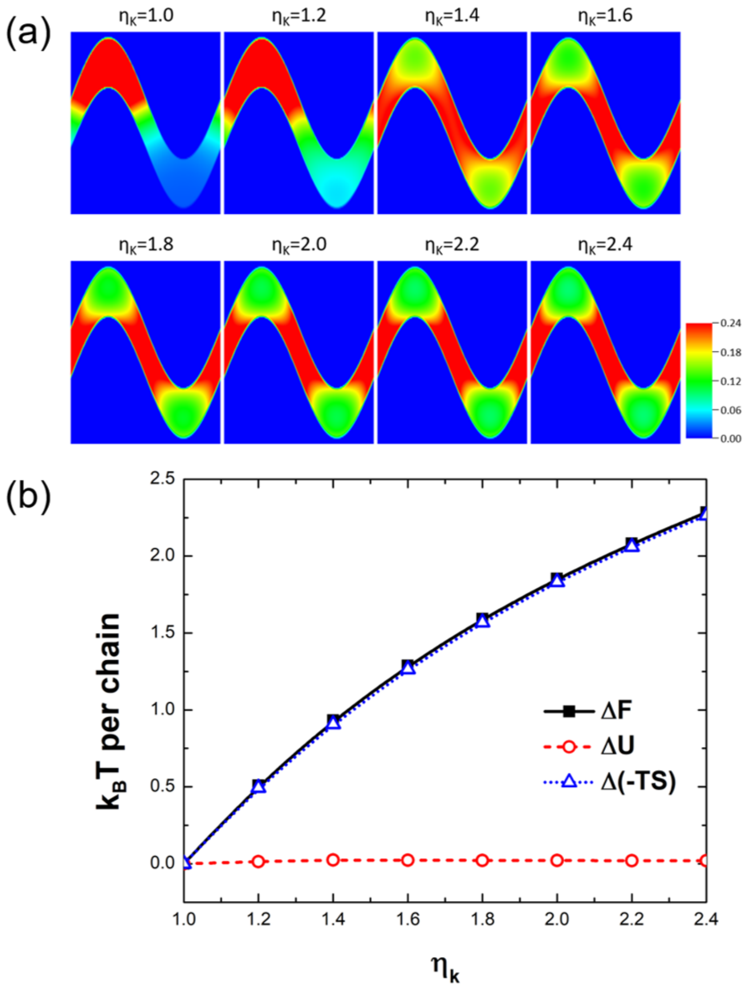

Figure S1: (a) SCFT density profiles of B polymers inside corrugated thin films for $\phi_B = 0.2$, $\chi = 0.1$, and $N = 60$ at various Kuhn length ratio η_K. The length scale is in units of $R_g = (N/6)^{1/2} l_A$, which is the radius of gyration of the A polymer. The corrugation is defined by a sinusoidal function, $u(x) = a \sin(2\pi x/\lambda)$, with $a = 1.0$ and $\lambda = 2.56$. The film thickness is dictated by the separation of the two sine waves, which is set as 0.8. (b) The change of overall free energy (ΔF), enthalpic term (ΔU), and entropic term ($\Delta(-TS)$, T is temperature) as a function of η_K for $\eta_K = 1$.

the B-rich phase is shifted to the slope region where the curvature is lower. This results in the A polymers being accommodated in the high curvature region. The change in system configuration is to reduce the entropy loss as a result of the confining segments with the larger Kuhn lengths in the high curvature region. This overcomes the effects from two other factors, namely, the entropy loss from confining a portion of A polymers in the high curvature region and the slight increase of enthalpy due to an increase in the interfacial area between A and B (see Fig. S1(b)). This lateral domain redistribution clearly demonstrates the sorting effect induced by the coupling of spatial curvature and polymer conformational asymmetry.

2.2 Geometric consideration

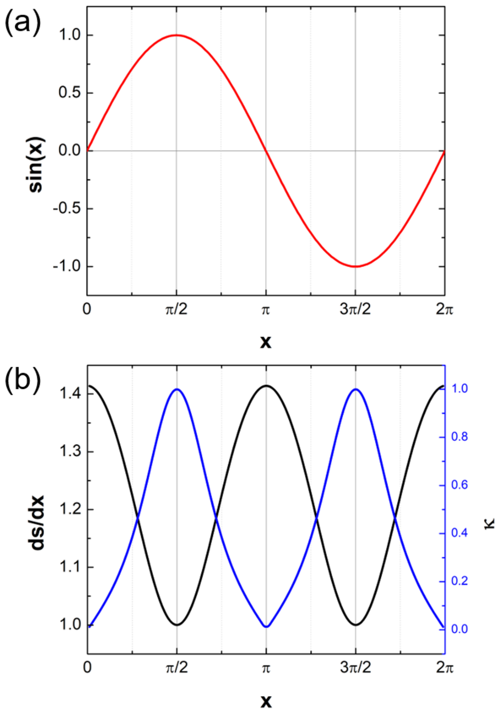

Figure S2: Illustration of (a) $\sin(x)$ curve in the range of $[0, 2\pi]$ and (b) associated geometric properties that includes the slope of the arc length, $\mathrm{d}s/\mathrm{d}x = \sqrt{1+\cos^2 x}$ (black curve), and the corresponding curvature $\kappa = |\sin x|/(1+\cos^2 x)^{3/2}$ plotted on a separate y axis (blue curve).

2.3 Density profiles of different B volume fractions

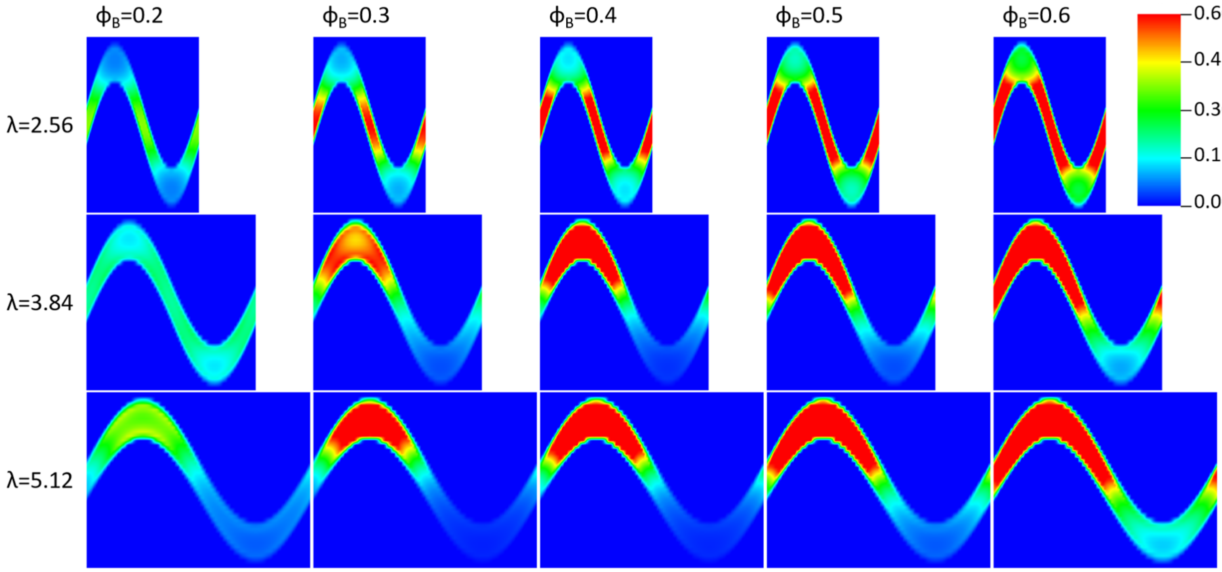

Figure S3: SCFT density profiles of B polymer inside sinusoidally corrugated thin films of $a = 1.4$ for $\chi = 0.1$, $N = 60$, and $\eta_K = 2$ at various corrugation wavelengths λ and volume fractions ϕ_B. The length scales are in units of $R_g = (N/6)^{1/2} l_A$, namely the radius of gyration of the A polymer.

3 Supplementary Molecular Dynamics (MD) Results

3.1 Coarse-grained model and simulation procedure

We adopted a coarse-grained model with implicit solvent based on the Cooke–Deserno lipid model.[2,3] As illustrated in Fig. S4(a), a lipid is represented by three beads connected *via* anharmonic springs, which can be made stiff or rod-like with the addition of an angle potential (see Eqs. 1-4 in Ref. 4). The tail beads have a diameter σ and the head beads are of size $0.95\ \sigma$. The head bead is purely repulsive while the pair-wise interaction between tail beads consists of a hard-core repulsion and a long-range attraction that is dictated by a decay parameter w_c.[4] This attractive long-range potential qualitatively prescribes the correct hydrophobic balance. We empirically determined the relationship between w_c and the bending rigidity κ of the lipid bilayer, which is given by $\kappa = \mathrm{e}^{\,8.051 w_c - 9.730}$.[4] The corrugated substrate was composed of a group of fixed beads with a thickness of $5\ \sigma$ and a number density of $1\ \sigma^{-3}$ (see Fig. S4(b)). The substrate surface conformed to a sine wave function along the x direction, $u(x) = a \sin(2\pi x/\lambda)$ ($a = 0$ represents a planar substrate). The related plots were all shifted in phase for illustration purpose. Given the translational symmetry imposed in the y direction, the corresponding principal curvature is equal to zero, hence the Gaussian curvature of the surface is also zero.

The initial setup of the simulation box is shown in Fig. S4(c), which has dimensions of $L_x = L_y = 40\pi\ \sigma$ and $L_z > 120\ \sigma$. Periodic boundary conditions were enforced in both the x and y directions. The z component of the center-of-mass of the substrate was located at $-2.5\ \sigma$, and the reference line of the surface wave pattern was at $z = 0$. A lipid bilayer with randomly distributed lipids was arranged in a cylindrical arc with angle θ and radius R, which was positioned with its lowest point $2\ \sigma$ above the nearest peak of the corrugated substrate. The arc length of the cross-section S was equal to the arc length of the substrate surface. The average area per lipid was set to $1.35\ \sigma^2$, which is near to the equilibrium value for the Cooke lipids of $w_{c,AB} = 1.3\ \sigma$.[2–4] We note that by using a higher value of area per lipid, one could

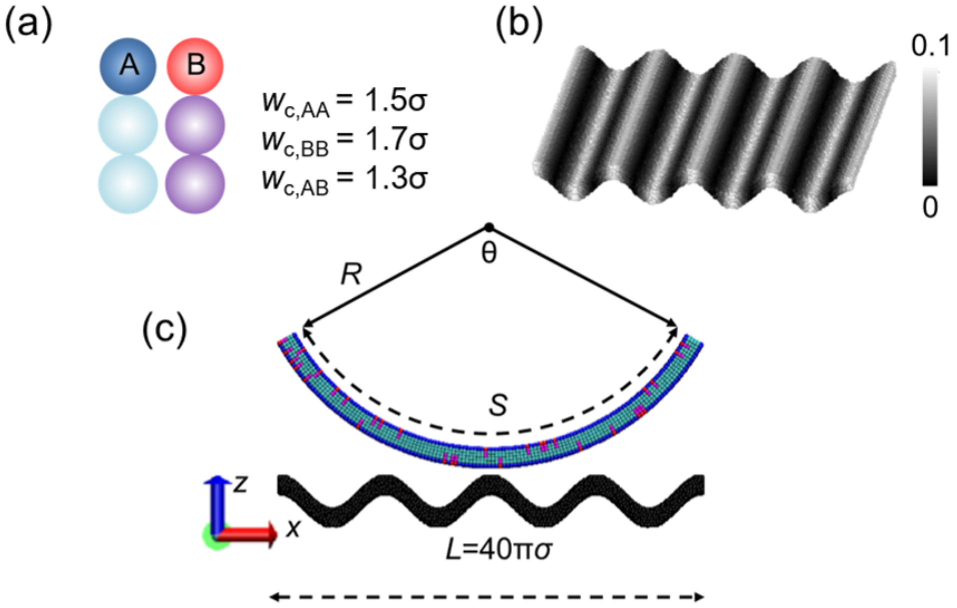

Figure S4: (a) Illustration of the coarse-grained model for A and B lipids, showing blue and cyan beads for the head and tail of A lipid, respectively, and red and magenta beads for the head and tail of B lipid, respectively. The parameters $w_{c,AA}$, $w_{c,BB}$, $w_{c,AB}$ are the tail-tail interaction parameters for A-A, B-B, and A-B types of interactions, respectively. (B) Illustration of the substrate consisting of fixed beads, which conforms to a sine wave function. The gray-scale legend pertains to the absolute value of the mean curvature for the case of $a = 5\ \sigma$ and $\lambda = 10\pi\ \sigma$. (c) Initial setup of the simulation, where the lipid bilayer is arranged on a cylindrical arc with radius R and angle θ. The arc length S is equal to the length of the substrate surface.

minimize buckling and imperfect coating of the bilayer onto the substrate. In the bilayer, the major component was the A lipid, which has a tail-tail interaction parameter $w_{c,AA} = 1.5\ \sigma$ that results an *empirical* bending rigidity $\kappa_A = 10.4\ k_BT$ (k_BT is thermal energy), while the minority B lipids were stiffer with $w_{c,BB} = 1.7\ \sigma$, corresponding to $\kappa_B = 52.3\ k_BT$. These w_c values were chosen such that the lipid membrane is in the fluid phase.

A harmonic spring potential, $U_{sp} = k_s[z_{cm} - (a+\sigma)]^2/2$, was applied to the lipids in the initial configuration to move the bilayer towards the substrate, where z_{cm} is the z component center-of-mass of the bilayer and the spring constant $k_s = 2000\ k_BT/\sigma^2$. The pair interaction between substrate and lipid beads is described by a truncated-shifted Lennard–Jones (LJ) potential,

$$U_{LJ} = \begin{cases} 4\varepsilon_{LJ}\left[\left(\frac{\sigma}{r_{ij}}\right)^{12} - \left(\frac{\sigma}{r_{ij}}\right)^{6} - \left(\frac{\sigma}{r_c}\right)^{12} + \left(\frac{\sigma}{r_c}\right)^{6}\right] & r_{ij} \le r_c \\ 0 & r_{ij} > r_c \end{cases} \tag{S12}$$

where r_{ij} is the distance between the i and j beads, σ is the bead diameter, r_c is the cut-off distance, and ε_{LJ} is the potential well-depth. Specifically, $\varepsilon_{LJ} = 0.75\ k_BT$ and $r_c = 2.5\ \sigma$ for the attractive interaction between substrate and head beads; $\varepsilon_{LJ} = 1.0\ k_BT$ and $r_c = 2^{1/6}\ \sigma$, namely, the Weeks–Chandler–Andersen (WCA) potential for the purely repulsive interaction between the substrate and tail beads. This interaction setup allows the formation of a perpendicular bilayer on the substrate.

Standard LJ reduced units were used and all quantities were nondimensionalized with respect to the length σ, energy ε, and mass m. Accordingly, the reduced time is $\tau = \sigma\sqrt{m/\varepsilon}$ and temperature is $T = \varepsilon/k_B$ (k_B is the Boltzmann constant). The length and time units are approximately 1 nm and 10 ns, respectively in real units.[2] Canonical ensemble simulations were performed using a Langevin thermostat with a friction coefficient of $1.0\tau^{-1}$, and the equations of motion were integrated with a timestep of 0.01τ using the velocity-Verlet algorithm implemented in the LAMMPS MD simulations package.[5,6] The initial run proceeded up to 5000 τ, while the production run proceeded up to $8 \times 10^5\ \tau$, which is approximately 8 ms in real units. Sample LAMMPS input and data files for the initial film lamination process and the succeeding coarsening production runs are provided at `https://code.ornl.gov/jyw/influence-of-curvature-on-domain`. The statistical results were obtained from three independent simulation runs. Table S1 tabulates the simulation system sizes for different substrate wavelengths, λ.

Table S1: System sizes

λ	${n_{Atom}}^{a}$	${n_{Substrate}}^{b}$	${n_{Lipid}}^{c}$
10π	176,171	79,451	32,240
20π	164,234	79,418	28,272
40π	160,244	79,148	27,032
∞	157,025	77,417	26,536

[a] total number of beads
[b] number of substrate beads
[c] number of lipid molecules

3.2 Domain discretization for data analysis

The binary system forms separate B lipid domains along with the simulation. The data analysis relies on the characterization of the phase-separated domains. As illustrated in Fig. S5, the numerical analysis is performed over a 63×63 mesh encompassing the substrate, with a grid size of $\Delta x_i = \int_{x_i}^{x_{i+1}} \sqrt{1 + (2\pi a/\lambda)^2 \cos^2(2\pi x/\lambda)} \mathrm{d}x$ (*i.e.*, the arc length from indexes x_i to x_{i+1}) and $\Delta y_j = \Delta y = 40\pi\ \sigma/63 \approx 1.995\ \sigma$. The grid surface area is approximated as $\Delta A_i = \Delta x_i \Delta y$. The identity of a grid is defined by the majority species inside the grid.

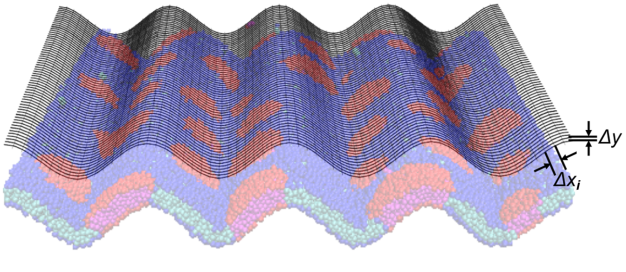

Figure S5: Illustration of a 63×63 mesh used in data analysis, with grid size Δx_i and Δy.

Domains are formed by neighboring grids having the same identity, which are identified from the system configuration. The domain grid members are tracked by a linked list through cluster analysis.[7] We focus on the separate B lipid domains, where the number of domains n_d and the area of each domain $A_d = \sum^d \Delta A_i$ (d is the number of grids in a domain) are determined along the simulation trajectory. The total perimeter length of the domains l_b was estimated by summing Δx_i and Δy for all pairs of nearest neighbor grids with different identities.

3.3 Brief kinetic analysis

We first checked the phase separating process of binary lipid mixtures supported by a planar substrate. The simulation trajectories (of the production runs) were analyzed to understand the demixing behavior inside the bilayer. Fig. S6 shows the statistical results from the ensemble average. As the simulation proceeded and the coarsening of B domains took place, the number of B lipid domains n_d and the total boundary length of B lipid domains l_b decreased (Fig. S6(a) and (c)); the average area of the B lipid domains increased (Fig. S6(b)). This coarsening process acts to reduce the interfacial energy between the A and B lipids at the domain boundaries, which is proportional to the total boundary length.[8]

Next, we examined the effect of surface corrugation on the evolution of the phase separation in the bilayer. In Fig. S7, we show the temporal evolution of n_d, A_d, and l_b, in the system with $\rho_B = 0.15$ and with different surface corrugations – the flat substrate ($a = 0$) case is included for comparison. The system forms large B lipid domains on the flat substrate, and exhibits the largest A_d, and the smallest n_d and l_b in the steady state. As the substrate becomes corrugated, intermediate-sized B lipid domains get trapped in low curvature regions, which hinders the coarsening process. Therefore, as λ reduces and the curvature effect increases, n_d comparatively increases, while A_d decreases and l_b increases.

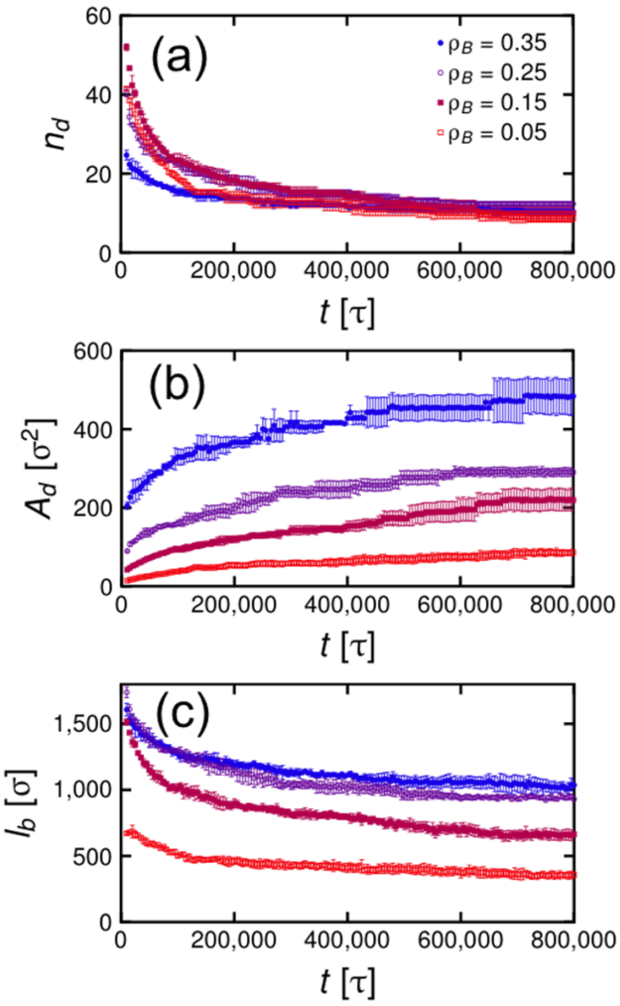

Figure S6: The temporal evolution of (a) number of domains n_d, (b) average area per domain A_d, and (c) total boundary length between domain and matrix l_b, in a phase-separating binary mixture supported by a planar substrate with a different B lipid number fraction ρ_B.

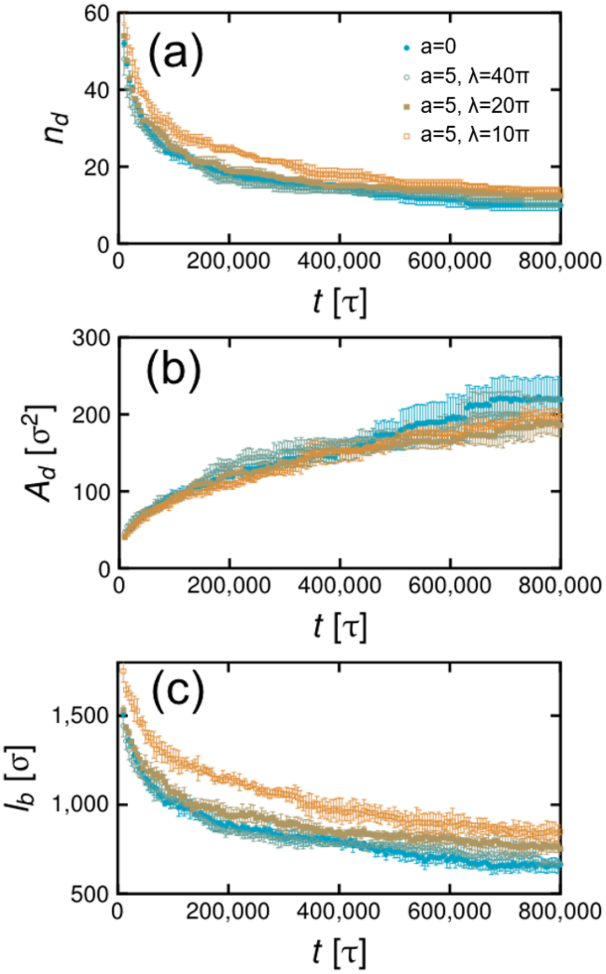

Figure S7: The temporal evolution of (a) number of domains n_d, (b) average area per domain A_d, and (c) total boundary length between domain and matrix l_b, in a phase-separating binary mixture of $\rho_B = 0.15$ supported by substrate with different surface corrugations.

3.4 Average mean curvature and domain area

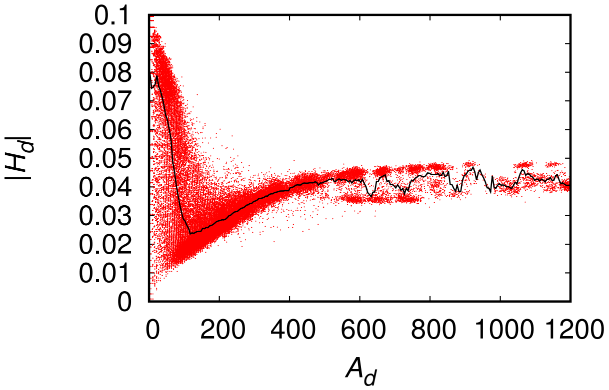

Figure S8: Distribution of average domain mean curvature $|H_d|$ as a function of domain area, A_d, for a system with $a = 5$, $\lambda = 10\pi$. The red data points are the aggregate data from three independent runs of systems with different ρ_b and at different times in the simulation trajectory. The black line is the binned data for bin size in the x-axis equal to 5 σ^2.

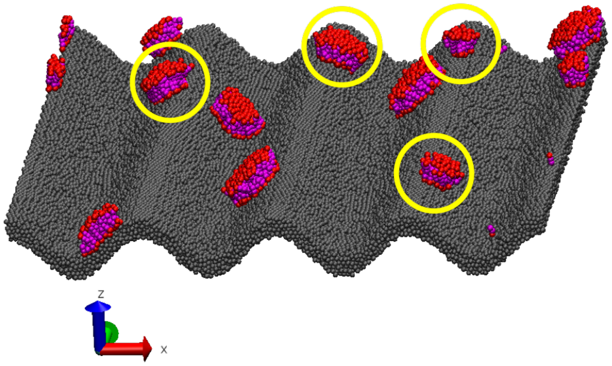

Figure S9: Snapshot of the final simulation frame at $t = 8 \times 10^5\ \tau$ for the system with $\rho_B = 0.05$. Domains that are situated at high curvature regions are encircled.

3.5 Line tension between A and B domains

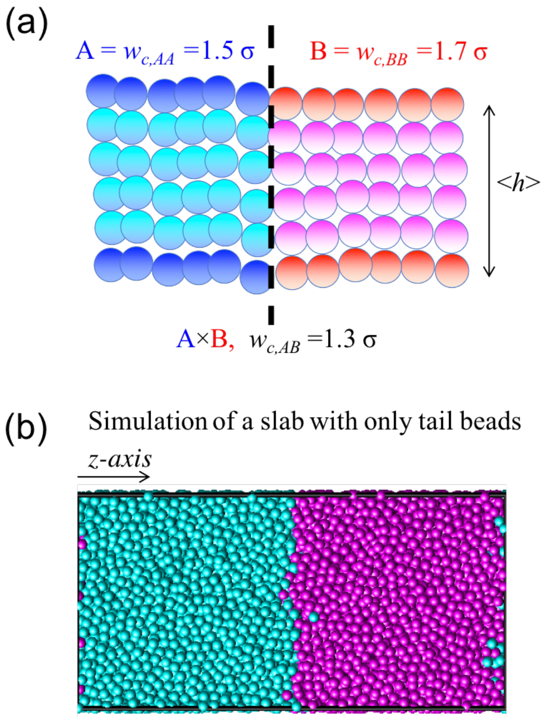

Figure S10: (a) Schematic of the domain interface between A and B lipids shown as a dotted line, and where the parameters of the Cooke-Deserno model[2,3] are also indicated. (b) Snapshot of the MD simulation of two slabs of A and B lipid tail beads.

The line tension between A and B domains is estimated by calculating the surface energy in their interface shown in Fig. S10(a). Since in the Cooke-Deserno model,[2,3] the head beads are purely repulsive, the main contributors to the interfacial energy are the tail beads. We performed MD simulations of a slab consisting of only A and B lipid tail beads (see Fig. S10(b)) and calculated the interfacial energy between two slabs as, $\gamma_s = L_z/2\,[\langle P_{zz}\rangle - (\langle P_{xx}\rangle + \langle P_{yy}\rangle)/2]$ where $\langle P_{xx}\rangle$, $\langle P_{yy}\rangle$, and $\langle P_{zz}\rangle$ are the average diagonal components of the pressure tensor and L_z is the length of the simulation box.[9] The line tension is then estimated as $\Sigma_{AB} = \gamma_s\,\langle h\rangle$, where $\langle h\rangle$ is the average thickness of the bilayer. For the parameters used in the simulations, $\Sigma_{AB} = 3.56\ k_BT/\sigma$.

References

(1) Tang, H.; Freed, K. F. Free Energy Functional Expansion for Inhomogeneous Polymer Blends. *J. Chem. Phys.* **1991**, *94*, 1572–1583.

(2) Cooke, I. R.; Deserno, M. Solvent-Free Model for Self-Assembling Fluid Bilayer Membranes: Stabilization of the Fluid Phase Based on Broad Attractive Tail Potentials. *J. Chem. Phys.* **2005**, *123*, 224710.

(3) Cooke, I. R.; Kremer, K.; Deserno, M. Tunable Generic Model for Fluid Bilayer Membranes. *Phys. Rev. E* **2005**, *72*, 011506.

(4) Carrillo, J.-M. Y.; Katsaras, J.; Sumpter, B. G.; Ashkar, R. A Computational Approach for Modeling Neutron Scattering Data from Lipid Bilayers. *J. Chem. Theory Comput.* **2017**, *13*, 916–925.

(5) Brown, W. M.; Wang, P.; Plimpton, S. J.; Tharrington, A. N. Implementing Molecular Dynamics on Hybrid High Performance Computers–Short Range Forces. *Comp. Phys. Comm.* **2011**, *182*, 898–911.

(6) Plimpton, S. Fast Parallel Algorithms for Short-Range Molecular Dynamics. *J. Comp. Phys.* **1995**, *117*, 1–19.

(7) Rapaport, D. *The Art of Molecular Dynamics Simulation*; Cambridge University Press, 2004.

(8) Różycki, B.; Weikl, T. R.; Lipowsky, R. Stable patterns of membrane domains at corrugated substrates. *Phys Rev Lett* **2008**, *100*, 098103.

(9) Kirkwood, J. G.; Buff, F. P. The Statistical Mechanical Theory of Surface Tension. *J. Chem. Phys.* **1949**, *17*, 338–343.